ALMA Study Project Report: Full-Mueller Mosaic Imaging With ALMA

S. Bhatnagar (PI)[1], P. Jagannathan[1], S. Sekhar[1,2], B. M. Kirk[1], C. Hull[3], P. Cortez[3], S. Kameno[3], E. Fomolant[3], T. Hunter[4], and C. Brogan[4]

[1]National Radio Astronomy Observatory, Socorro, US
[2]Institute for Data Intensive Astronomy, Univ. of Cape Town, SA
[3]National Radio Astronomy Observatory, Santiago, Chile
[4]National Radio Astronomy Observatory, Charlottesville, US

Feb., 2021

Executive Summary

This report describes the work carried out for the ALMA Study Project titled "Full-Mueller Mosaic Imaging with ALMA". The primary goals were to develop a model for the antenna primary beams (PB) in full-polarization, characterize the effects of the uncorrected in-beam polarization on full-polarization mosaic imaging and explore possible calibration and imaging algorithmic solutions.

Context: The effects of off-axis polarization leakage (a.k.a. "in-beam leakages") due to antenna primary beam (PB) are typically small at the center of the PB and increase in magnitude away from the center. For homogeneous arrays where these in-beam leakage patterns are assumed to be the same for all antennas in the array, correction for these in-beam leakages for the *static* case (small or no temporal variations of the full-polarization PB) has been done post-imaging by dividing the final image with a model of the full-Stokes PB. For heterogeneous arrays where the in-beam leakages vary with antenna, time and frequency, post-imaging corrections needs to be done as part of the imaging process. Wide-field/mosaic imaging in full-polarization therefore requires an accurate measurement of the antenna PB(s) in full polarization, and an imaging algorithm that utilizes the knowledge of the antenna PBs to correct for the effects of the PBs including in-beam polarization leakages. The *A-Projection* algorithm for imaging is one such algorithm, which requires an accurate model for the PB. Measurements of the antenna PBs using the holographic measurement technique, characterizing the effects of the in-beam polarization leakage on full-Stokes wide-field/mosaic imaging with ALMA and developing a model for the full-Stokes PB were the primary goals of this Study Project. Results from this project will now allow estimation of the field-of-view (FoV) which can be imaged before errors due to the off-axis polarization effects dominate. The study also explored the algorithmic R&D path for enabling the full-Stokes mosaic imaging, thus widening the FoV and increasing the speed of wide-field/mosaic imaging.

Astroholography (Band-3) : Drift scan astroholography data using a bright quasar with radial scanning pattern across the antenna aperture were taken (in 2015) prior to the start of this study in Bands 3,4 and 6. These data were re-processed using *standard CASA tasks and tools*. This allowed us to quantitatively review the conclusions of existing reports. We concluded that new holography data is necessary due to the use of the drift scan mode for these observations and radial scanning pattern, both of which are sub-optimal. Reprocessing of the 2015 data showed that

only Stokes-I beam measurements are reliable. For reasons not quite clear, the Stokes V←I and U←I leakage maps are too noisy and show un-physical structure. Late in this Study Project (Oct. 2018) we were able to acquire new holography data in ALMA Band 3, using a rectangular grid scanning pattern. These data were also analyzed as part of the work for this project.

The new data has good signal-to-noise ratio (SNR) to measure the PB out to the 4^{th} sidelobe and show reliable PB maps in all Stokes. The Stokes-I and V←I maps from 2015 and 2018 data are similar in magnitude and structure. The Stokes-I PB shows the azimuthal asymmetry (due to feed support structures and the secondary reflector blockage) in the main-lobe and in the sidelobes. Stokes Q←I and U←I patterns show the familiar quad-polar pattern (a.k.a. the "Clover leaf" pattern) and V←I pattern shows the bi-polar pattern of opposite polarity.

Antenna-to-antenna variations: The beam patterns show the expected differences with antenna types (DA-, DV-type). Residual antenna pointing offsets were found, after correcting for the pointing offsets from reference pointing observations as part of the standard ALMA data observing procedure. These residual pointing offsets are in the range of $12-15\%$ of the HPBW. After correcting for these residual offsets, the resulting PB show a significant imaginary part indicating that the antenna aperture illumination pattern (AIP) are only approximately Hermitian[1]. The measured AIPs show an offset in the AIP, and the offset varies with antenna. This is consistent with earlier similar analysis by Kundert et al. (2017). While this conclusion needs further investigation, if correct, this will cause degradation in imaging performance and higher than expected noise in the images (Kundert et al. 2017).

Polarization leakage patterns in Stokes-Q, -U and -V were measured for individual DV and DA antennas. The peak fractional leakages are in the $2-6\%$ range and occur within the PB main lobe where the PB response is in the $20-80\%$ range. Similar level of difference between antennas of the same type is also present (see Tables 2.1 and 3.1). Morphological differences between the two group of antennas is starker, some of which may be expected due to different optics in the two antenna types (see Figs. 4.2 and 4.1). Our assessment is that these differences will require heterogeneous array treatment for full-Stokes imaging.

Having followed the ALMA polarization calibration procedure, we find unexpectedly large Stokes-U at the center of the beam and more than expected antenna-to-antenna variations in Stokes-V patterns. These will require further effort to identify any possible issues in the calibration (see Sec. 2.4.1).

Effects on imaging performance: Peak in-beam leakages within the HPBW for many antennas is comparable to the typical fractional sky brightness in Stokes-Q, -U and -V parameters. This can lead to errors of up to 100% in the full-Stokes flux vector. The overall imaging performance is a strong function of the accuracy of prediction step in iterative algorithms. While the image-plane may offer some reduction in the *apparent* leakages due to averaging of various antennas, no such averaging over antennas occurs in the prediction step. The measured antenna to antenna variations suggest that unless corrected for, image fidelity may also be adversely affected. Precise characterization of the effect on the imaging dynamic range however needs careful simulation and on-sky test (see also Kundert et al. (2017) for similar independent estimates).

PB modeling: The *A-Projection* algorithm for wide-field full-Stokes imaging requires a model for the AIP. The technique of modeling the Zernike polynomial modeling of holographically measured AIPs and the associated software were developed as part of this study project. While the *A-Projection* algorithm only needs the AIP models, the models were converted to full-Stokes antenna far-field voltage patterns (VP) and antenna PBs. We find that the Zernike polynomial models do capture most of the features expected from fundamental antenna optics in all the elements of the 2×2 direction-dependent antenna Jones matrix.

[1]Mathematically, the real part is an even function while the imaginary part is an odd function. Fourier transform of such functions is real-valued.

Algorithms and Software : A suite of Python-based software was developed for end-to-end processing of holography data using the *standard* tools and tasks in the CASA package as part of this project. This was successfully used to process old data (from 2015) and new data (from 2018) for holography and for evaluating TICRA models. A different software system was also developed to solve for the Zernike models, given the derived antenna-based complex AIPs in full polarization. The software can be configured to generate an average model for each antenna type, or a separate model per antenna or to average along the frequency axis (to improve SNR in the measurements). All of this software is currently available as a Git repository and can be polished for a general release depending on demand and available time for the work required to make it production quality.

Recommendations:

1. A larger than anticipated fraction of time during this study project had to be devoted on re-acquiring holography data, developing the necessary software and building the beam models. While assessment was possible of the impact on wide-field full-polarization imaging with ALMA using these models, more work is necessary for software development and on-sky imaging tests before this imaging mode is released for general use. We recommend adequate resources be devoted for this followup work.

2. The full-Stokes PB models developed as part of this project represent the direction dependent off-axis leakages, and are a prerequisite for characterizing the full impact on wide-field full-Stokes imaging performance. We estimate that, if not accounted for, this may limit the accuracy and fidelity of full-Stokes imaging. It is strongly recommended that these results be verified and the inconsistencies between the results here and in the literature be fully understood first. Enabling wide-field full-Stokes imaging with ALMA for general scientific use will therefore require more development effort. We therefore strongly recommend that adequate resources be invested for this effort, and the issues in full-Stokes imaging better understood and characterized before enabling it for general scientific use.

3. We recommend that reliable and reproducible astroholography be available before moving to the next phase of using the results for full-Stokes wide-field imaging. We therefore recommend that adequate resources be devoted for making our modified scripts for holography observations production-ready and an observatory-supported regular holography mode of observing be enabled for ALMA. Furthermore, the necessary observing time should be allocated for holography measurements to track changes (e.g., due to antenna movement, feed changes/adjustments, other maintenance activities that can affect the full-Stokes PB, etc.). We also recommend that future holography observations be done using pointed observations on a *regular grid* (not the OTF mode for antenna motion in a star pattern).

4. We recommend that adequate resources be devoted on the post-processing front for both, R&D and making production-ready software. The software developed as part of this project uses the released CASA package for end-to-end processing of holography data. More effort is however necessary to make a holography pipeline using this software – something that will also be necessary for observatory-supported regular holographic measurements. More R&D is also necessary to properly characterize the effects of the PB in general and of the off-axis leakages in particular, develop software for full-Stokes corrections and estimate the associated cost of computing.

5. Full-Stokes beam using the TICRA models were also derived. While the shapes of the Stokes-I PB look reasonable, shapes for other Stokes parameters do not (in particular for Stokes-Q and -U). Numerically these patterns are about two orders of magnitude lower than our measurements and the models exist only as pixelated CASA images for an ideal antenna illumination pattern. These models therefore do not capture antenna-to-antenna variations or variations as function of frequency. We therefore do not intend to use these models for ALMA with the *A-Projection* algorithm to correct for the effects of the off-axis leakages in wide-field imaging.

Contents

List of Figures

List of Tables

Chapter 1

Introduction

The primary focus of this study project is to measure and characterize the effects of direction dependent off-axis polarization leakage of the antenna beam on mosaic/wide-field imaging with ALMA. Data for mosaic imaging involves pointing the telescope at multiple locations. Since the area imaged is larger than the field of view (FoV) of individual antenna, gain variations due to the shape of the antenna PB is imprinted on the mosaic image. The brightness distribution at any location within the imaged region gets contributions from the inner regions of the antenna PB from some pointings, and from the outer regions of the PB from the neighboring pointings. Hence, unlike in single pointing imaging where the emission near the center of the PB main lobe is largely unaffected by the direction-dependent effects of the PB, no part of a mosaicked image is free of the effects of the *entire* PB. This includes effects of gain variations within the main lobe and the first few sidelobes of the PB, time varying direction dependent gains due to rotation with Parallactic Angle (PA) or time-dependent antenna pointing errors and variations of the PB shape with frequency and polarization. Measuring the antenna PBs and an imaging algorithm to correct for all of these effects are therefore the fundamental prerequisites for wide-field imaging in general and mosaic imaging in particular. ALMA is a heterogeneous array with 3 different types of 12m antenna (DV, DA and TP) with significantly different beam shapes due to different feed-arm designs. PBs of all the different types of antennas therefore need to be measured separately and the imaging algorithm generalized to correct for appropriate PB for the baselines between the various different antenna types. The nominal pattern of the leakage of the Stokes-I flux into Stokes -Q, -U and -V is directionally more complex and significant relative to the typical magnitude of the Stokes-Q, -U and -V flux. Stokes-Q and -U beams fundamentally have a quarter-polar pattern with alternating polarity while the Stokes-V PB has a bipolar pattern of opposite polarity. Corrections for these off-axis effects is therefore even more crucial for full-Stokes mosaic imaging.

The imaging equation for full-Stokes imaging, including the effects of the PB can be written in terms of antenna-based direction-dependent matrices as:

$$\begin{aligned} \mathsf{I} &= \sum_{ij} \mathsf{S} \left[\mathsf{E}_i \otimes \mathsf{E}_j^* \right] \mathsf{I}^{sky} \\ &= \sum_{ij} \mathsf{S}\, \mathsf{M}_{ij}\, \mathsf{I}^{sky} \end{aligned} \tag{1.1}$$

where I^{sky} and I are the true and the observed Stokes image vectors. E_i are the antenna-based 2×2 matrices of the antenna far-field voltage patterns given by:

$$\mathsf{E}_i = \begin{bmatrix} \mathsf{E}^x & -\mathsf{E}^{x \to y} \\ \mathsf{E}^{y \to x} & \mathsf{E}^y \end{bmatrix} \tag{1.2}$$

The diagonal elements are the far-field electric field pattern (EFP) in the two orthogonal polarizations and the off-diagonal elements represent the leakage of the signal from one polarization into the other. $\mathsf{M}_{ij} = \mathsf{E}_i \otimes \mathsf{E}_j^*$, is the 4×4

Mueller matrix in the feed basis (linear polarization basis for ALMA) and S is the 4×4 matrix that transforms M_{ij} from the feed- to the Stokes-basis.

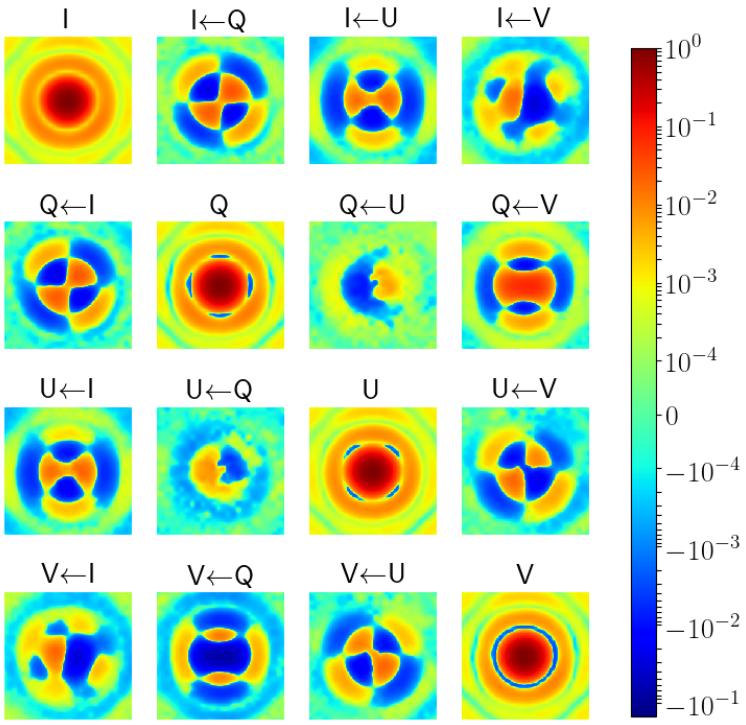

Figure 1.1: **Stokes-basis Mueller Matrix:** Shown in this figure is the direction dependent Stokes-basis Mueller Matrix (SM_{ij}) for the DV antennas of ALMA derived from holographic measurements taken in October 2018. Each element of this matrix is an average of 2 GHz in frequency (centered around 108 GHz) and all DV antennas. The elements are in the Stokes basis – the natural basis for the sky brightness distribution – to illustrate the mixing of the various Stokes planes into each other due to antenna dish geometry. The terms along the diagonal represent the forward gain along any of the Stokes polarizations while the off-diagonal elements represent the mixing of polarizations.

A representative M_{ij} is shown graphically in Fig. 1.1 for conceptual understanding. The four diagonal elements are the forward antenna gain for the four Stokes parameters and are the standard PB pattern. The last three elements of the first row (or the first column) are the direction-dependent leakage patterns of Stokes-I flux leaking into Q ($I \leftarrow$U), U ($I \leftarrow U$) and V ($I \leftarrow V$) respectively. The effect of these terms *dominate* the in-beam polarization leakage due to antenna optics. The rest of this report therefore deals with measuring and modeling only these terms. We estimate that the effects of other terms is below the thermal noise limit for ALMA and can therefore be safely ignored[1].

1.1 Imaging algorithm

The measurement equation for data calibrated for direction independent (DI) terms but not for the direction-dependent effects due to the antenna PB can be written as:

$$\mathsf{V}_{ij}^{obs} = \int \mathsf{M}_{ij}(\vec{s})\, \mathsf{I}^{sky}(\vec{s})\, e^{2\pi i \vec{s}.\vec{b}_{ij}} d\vec{s} \tag{1.3}$$

[1]Some of the off-diagonal terms of M_{ij} not in the first row (or column) may have significant effect in the imaging of strongly polarized sky brightness distribution.

where V_{ij}^{obs} is the observed visibilities along a direction $\vec{s}$ with a baseline vector $\vec{b_{ij}}$ formed with two antennas designated by subscripts i and j. V^{obs} and I^{sky} are the full polarization vectors in the feed polarization basis. M_{ij} encapsulates the effects of antenna PBs including the in-beam polarization leakage. Since it appears inside the integral over $\vec{s}$ and mathematically indistinguishable from I^{sky}, post-imaging corrections for PB effects in general is fundamentally ruled out; *i.e.,* corrections for the direction-dependent effects of the antenna PB has to be done as part of the imaging process itself[2].

Equation 1.3 can be re-written as

$$V_{ij}^{Obs} = \left(\mathsf{A}_i \circledast \mathsf{A}_j^{*}\right) \star V^{\circ} \tag{1.4}$$

where V° is the Fourier transforms of I^{sky}. A_i is the Fourier transform of E_i and is the 2×2 direction-dependent antenna Jones matrices. Symbols $\star$ and $\circledast$ represent the convolution and outer convolution operators respectively. The *A-Projection* imaging algorithm (Bhatnagar et al. 2008) corrects for the effects of the antenna PBs by incorporating the effects of A_i during imaging. The *FM-A-Projection* algorithm is a generalization that corrects for the off-axis PB leakage by potentially accounting for the full Mueller matrix (Jagannathan et al. 2017). The fundamental prerequisite for full-polarization mosaic imaging with ALMA is therefore the measurement of the antenna AIPs, which forms the input for the *A-Projection* algorithm. This measurement can be done using the technique of holography where one measures the PB of individual antennas by scanning a source of emission with a subset of antennas in the array while the rest of the antennas are pointed at the source for the reference signal. The SNR in such observations is significantly lower than a typical science target observation. Therefore for use in the *A-Projection* algorithm without degrading the imaging performance requires building an accurate model for the AIPs.

In the following sections, we describe the work done as part of this study project to measure, characterize and model the antenna AIPs for ALMA.

[2]The only exception when post-imaging correction for PB is still possible is the static case where PB does not change with time (e.g. due to rotation with parallactic angle) or frequency.

Chapter 2

Astroholography

Astroholograhy observations were done as part of this project to measure the ALMA AIPs. Below is a brief description of the observing procedure and the data analysis done.

Astroholography to measure the antenna AIPs is a well established technique in radio astronomy (Bates 1971a,b). Antennas of an interferometric array are divided into two groups of antennas. One group of antennas, referred to as the "tracking antennas" track a celestial source of sufficient strength (typically a compact calibrater source) while the rest of the antennas, referred to as the "scanning antennas" scan the source. The measurement equation for such measurements is given by:

$$V_{TS}^{Obs} = \mathsf{F}\left(\mathsf{E}_T \otimes \mathsf{E}_S^*\right) \mathsf{I}^{sky} \tag{2.1}$$

where the subscripts T and S refer to the tracking and scanning antennas respectively. F is the Fourier transform operator and I^{sky} is the sky brightness distribution. I^{sky} here is a single unresolved source in the antenna FoV.

Data was collected for full polarization on-axis calibration using periodic visits to the central source which acts as the amplitude, phase and polarization calibrator. Calibration solutions were derived from the data on calibrators for antenna based complex gains and on-axis polarization leakages using the standard ALMA calibration procedure[1] and applied to the entire holography data set. The on-axis gain solutions from flux and phase calibrators correct for the diagonal elements while the on-axis leakage solutions from polarization calibrator(s) correct for the off-diagonal elements of E in Eq. 2.1. Since the source in the sky is always on-axis for the tracking antennas, this calibration process reduces E_T to an identity matrix. After calibration, elements of E_S from the various holography pointings have the measurements of the antennas based antenna EFPs. The diagonal elements measure the EFP for the two polarizations, while the off-diagonal elements measure the EFP of the off-axis fractional polarization leakages. The measurement equation for baselines between tracking (sub-script T) and scanning (sub-script S) antennas after calibration is therefore:

$$V_{TS}^{Calibrated} = \mathsf{F}\left(\mathbb{1} \otimes \mathsf{E}_S^*\right) \mathsf{I}^{sky} \tag{2.2}$$

Gridding $\sum_T V_{TS}^{Calibrated}\ \mathsf{I}^{sky^{-1}}$ for every pointing of the scanning antennas in the direction σ and polarization p on a grid gives the map of the nominal EFP for the scanning antenna S:

$$\mathsf{E}_S(\sigma, p) = \sum_T \left[V_{TS}(\sigma, p)\right]^{Calibrated} \left[\mathsf{I}(p)^{sky}\right]^{-1} \tag{2.3}$$

where the subscript p denotes the polarizations X or Y, or polarization leakages $X \rightarrow Y$ or $Y \rightarrow X$. These 4 elements of E_S for the averaged DV (16 antennas) and DA(18 antennas) ALMA antenna types are shown in Fig. 2.1. A second observation with the antennas in the scanning- and tracking-sets interchanged gives a measurement of the EFPs for all the antennas in the array.

[1]The ALMA calibration procedure used in this project is described in the CASA guides for ALMA calibration.

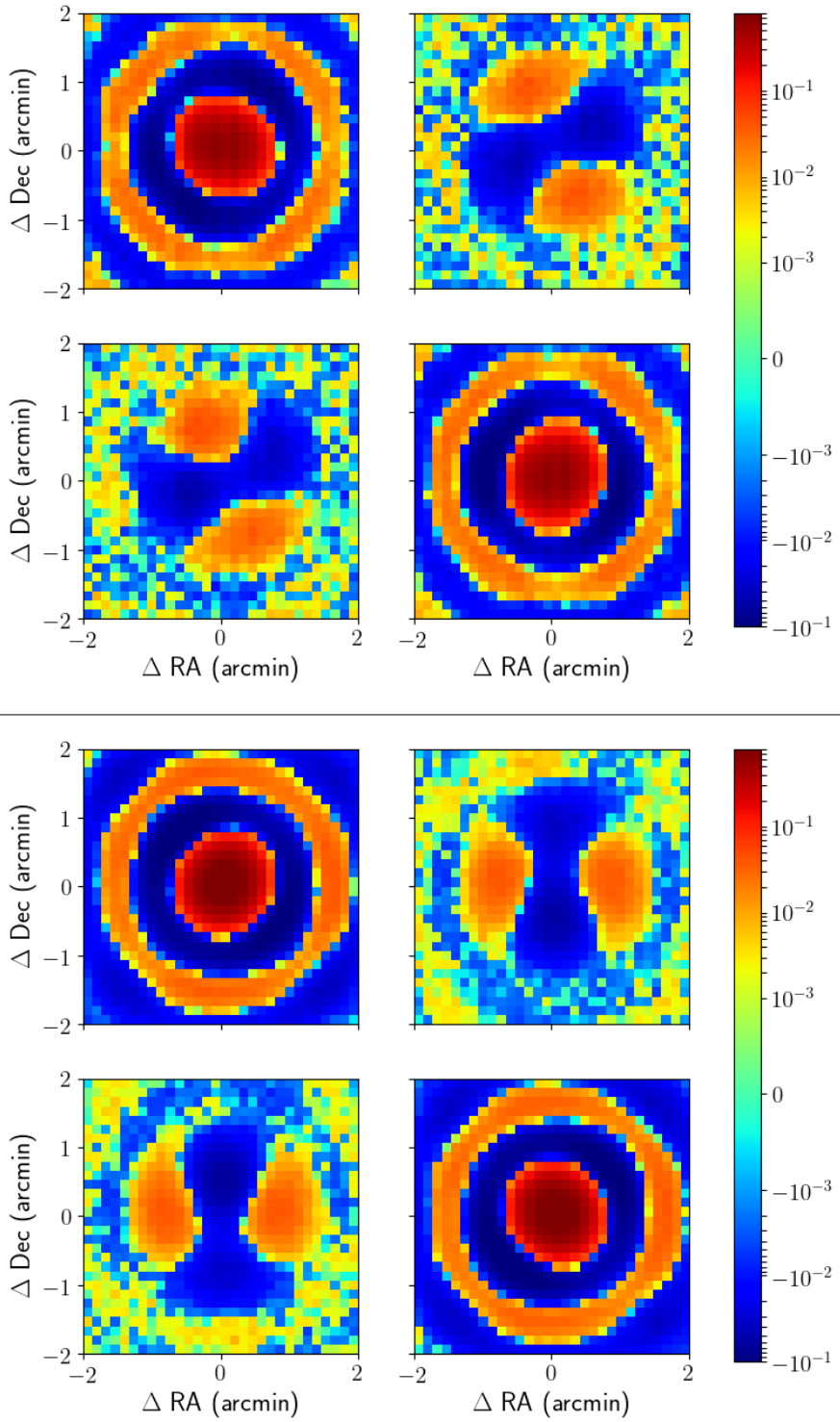

Figure 2.1: **Voltage patterns in the feed basis:** Holographic map of the real part of the antenna voltage pattern for ALMA **DV (images above the horizontal line)** and **DA (images below the horizontal line)** antennas in feed basis averaged over all antennas in each group and over 2 GHz of frequency band centered at the 108-GHz band (Band 3). The four set of images in the top panel (DV antenna) and bottom panel (DA antenna) show the X and X←Y patterns in the top row while the bottom row shows the patterns in Y←X and Y.

These direction-dependent Jones matrices can be used to compute antenna primary beams in the feed-basis as $\mathsf{E}_S \otimes \mathsf{E}_S^*$ (see Sec. 2.3 for details), which can converted to Stokes basis as

$$\mathsf{PB}_{stokes} = \mathsf{S}\left[\mathsf{E}_S \otimes \mathsf{E}_S^*\right] \tag{2.4}$$

The term in the square brackets is the Mueller matrix. The dominant off-axis leakage terms are in the first row (or column) of the PB matrix on the RHS. These terms in the Stokes basis specifically for linear feeds are given by:

$$PB_I = PB_{XX} + PB_{YY} \tag{2.5a}$$
$$PB_Q = PB_{XX} - PB_{YY} \tag{2.5b}$$
$$PB_U = PB_{XY} + PB_{YX} \tag{2.5c}$$
$$PB_V = PB_{XY} - PB_{YX} \tag{2.5d}$$

These terms for DV and DA antennas are shown in Figs. 2.3 and 2.4.

2.1 Scanning pattern

The accuracy of the shape of the PB measured using holographic techniques depends on the measurement noise and on the precise knowledge of the pointing direction of the scanning antennas. Noise is directly proportional to the strength of the signal (flux of the celestial source used), and inversely proportional to $\sqrt{N_T\, T_{int}}$ where N_T is the number of scanning antennas and T_{int} is the total integration time *per pointing*. The two dominant sources of errors in the pointing direction are the inherent antenna pointing accuracy and the uncertainty that may be introduced in mapping the data from the scanning pattern used in the measurements on to a regular grid (e.g., as shown in Fig. 2.1).

The antenna pointing errors can be measured via the standard reference pointing calibration procedure where the pointing errors are determined via line fits to few-pointing scan in the antenna Az-El plane. For holographic observations, one can also arrange to have the scanning pattern centered around the nominal optical axis of the antenna. The peak of the holographic maps away from this nominal on-axis pointing direction will then give a measure of the antenna pointing offset. Alternatively, a more accurate method to measure the antenna pointing offset can be via the measurement of the phase slope across the measured AIP.

2.1.1 The `star` pattern

There are *at least* three different scanning patterns in use that we are aware of. The ALMA holography data taken in 2015 used the "star" scanning pattern where a number of radial scans are made with each scan traversing the nominal on-axis direction as shown in Fig. 2.2. The holography pattern scanned was a series of radial slices 7.5 degrees apart in azimuth resulting in 48 slices. Each radial slice was sampled 16 times. A result of the chosen pattern is a sampling biased towards the center of the beam compared to the outer regions. Significantly larger fraction of the total observing time is therefore spent in the inner part of the beam, where the antenna gain is also relatively higher and simpler in structure. The outer parts of the beam, where the antenna gain is lower and where the PB structure is more complex is sampled relatively sparsely. As a result the parts of the PB where the SNR is inherently lower and where the PB structure is also more complicated is sampled relatively sparsely. The information about where the antennas are actually pointing was also not directly available in the 2015 observing mode. This information therefore had to be derived from the associated meta data, and is likely to have injected additional spatial noise. This adds additional uncertainty which is directly reflected in the structural accuracy of the PB maps. Finally, these data sampled only the main lobe (barely in some cases). As shown later, significant off-axis leakage extends beyond the main lobe in general.

2.1.2 The `regular grid` pattern

New holography data were taken in 2018 as part of this project where the pointings were on a regular grid. A series of linear scans about the nominal on-axis direction are made and data recorded at regular intervals. This pattern spends equal time in all parts of the PB with a uniform sampling density. While not optimal, this scanning pattern is an improvement in terms of uniform instrumental noise and in measuring the complex structure with denser set of pointing compared to the star pattern. Since the scanning pattern is already close to a regular grid, the uncertainty in mapping the data on to a regular grid is also significantly reduced. An optimal setup would be one which gives a uniform *SNR* across the PB. This can be achieved by weighting the integration time per pointing with the gain of the nominal PB. This would effectively produce data with larger integration time per pointing in the outer parts of the PB relative to the inner parts of the PB (where the complexity of the PB-structure is lower and the antenna gain is higher).

2.2 Noise budget

As mentioned earlier, the 2018 data was acquired with the antenna scanning the celestial source in a regular grid pattern of 7×7 points around the celestial source. The source used was J1924-2914 with a known time variable flux density of ~5.5 Jy at Band-3. However the antennas were still in the on-the-fly mosaic mode with 0.2915 seconds per grid point. This gives an instantaneous sensitivity of 73.7 mJy/baseline for 2 GHz of bandwidth at Band-3. There were 34 tracking antennas for our holographic observations with 16 DV and 18 DA antennas. For scan numbers 4,8 and 12 the DA antennas were used as reference antennas (always pointing at the source) and the DV as scanning antennas. For scan numbers 2,6 and 10 the DV antennas were used as reference antennas and the DA antennas were used as scanning antennas. This scanning strategy allowed us to generate a holographic map of all the antennas in the array from a single observation. The scans also spanned over 60 degrees in parallactic angle allowing for straight forward polarization calibration. The observing correlator setup had a 8 GHz bandwidth in the ALMA Band-3. In this report we focused on one TDM spectral window of2 GHz bandwidth centered at 108 GHz. Averaging all the

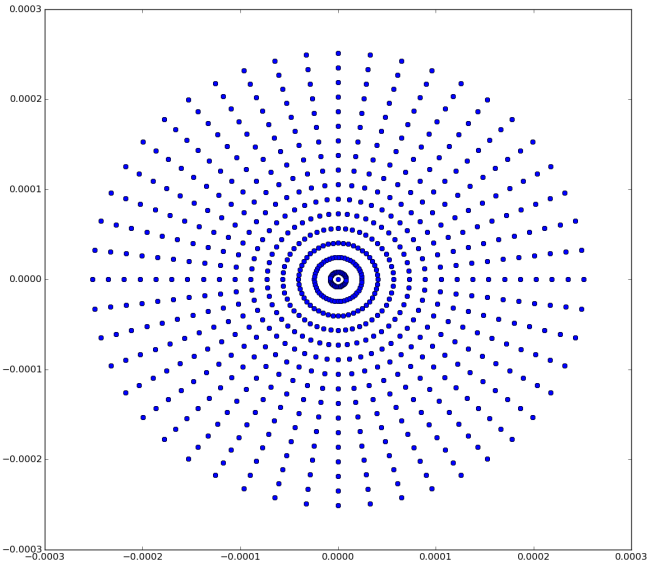

Figure 2.2: The `star` scanning pattern used for the 2015 holographic measurements.

baselines between a given scanning antenna to all the tracking antennas gives a sensitivity boost of a factor of 4 for the DV antennas and ~ 4.3 for the DA antennas. This gives a SNR of ~ 300 around the center of the beam.

After the averaging of the data with all the reference antennas and averaging across the frequency, the antenna patterns derived from the data however still had morphologically unexpected features. There was significant leakage at the bore-sight of the derived full Stokes beams for most antennas. It was ultimately determined that there were significant antenna pointing errors in the data, with significant variations across the antennas and across the observing band. The available SNR allowed us to determine a different antenna pointing offset for each scanning antenna, which we removed to ensure that the smearing of the beams due to these pointing offsets is minimal when averaging across antennas of the same type to derive an average beam.

The average Jones (EFP) and Mueller matrix terms (PBs) computed separately for the DA and the DV antennas are shown in Fig. 2.3 and correspond to an SNR of ~ 1200. These antenna-averaged EFPs $\overline{\mathsf{E}(\sigma,p)}$ are computed as

$$\overline{\mathsf{E}(\sigma,p)} = \frac{1}{N_S N_T}\sum_{S}^{N_S}\sum_{T}^{N_T}\left[V_{TS}(\sigma,p)\right]^{Calibrated}\left[\mathsf{I}(p)^{sky}\right]^{-1} \tag{2.6}$$

where N_T is 16 for DA and 18 for DV antennas. N_S is 18 for DA and 16 for DV. Figure 2.4 shows the same maps but interpolated using a cubic spline interpolation scheme. The individual frequency-averaged per antenna beams are shown in Appendix 4.2. The SNR in each of those maps is ~ 300.

2.3 Data processing

Data from both, 2015 and 2018 observations were calibrated following the standard manual polarization calibration procedure in CASA recommended by the ALMA project[2]. Standard calibration tools in CASA were used in a holography calibration pipeline, which was developed as part of this project. The pipeline script closely follows the calibration steps carried out by the ALMA polarization beam characterization report[3], with the difference being that we use the calibration tasks and tools within CASA[4]. Following are the steps in the pipeline script for calibration of holography data that we used:

- A-priori flagging
- Water vapor measurement corrections
- Combine executions for greater parallactic angle coverage
- Determine short-duration atmospheric gains (pre-bandpass)
- Determine antenna-based frequency gains (bandpass)
- Determine back-end electronics gains (cross-hand gains)
- Determine each antenna's XY-phase offset
- Recompute antenna gains now that source polarization is accounted for
- Determine polarization contribution of each antenna (polcal)
- Apply the calibration tables.

[2]The ALMA calibration procedure used in this project is described in the CASA guides for ALMA calibration.
[3]http://www.alma.cl/~skameno/AMAPOLA/PolarizedBeamProc.html
[4]The released CASA version 5.3 was used for processing the data

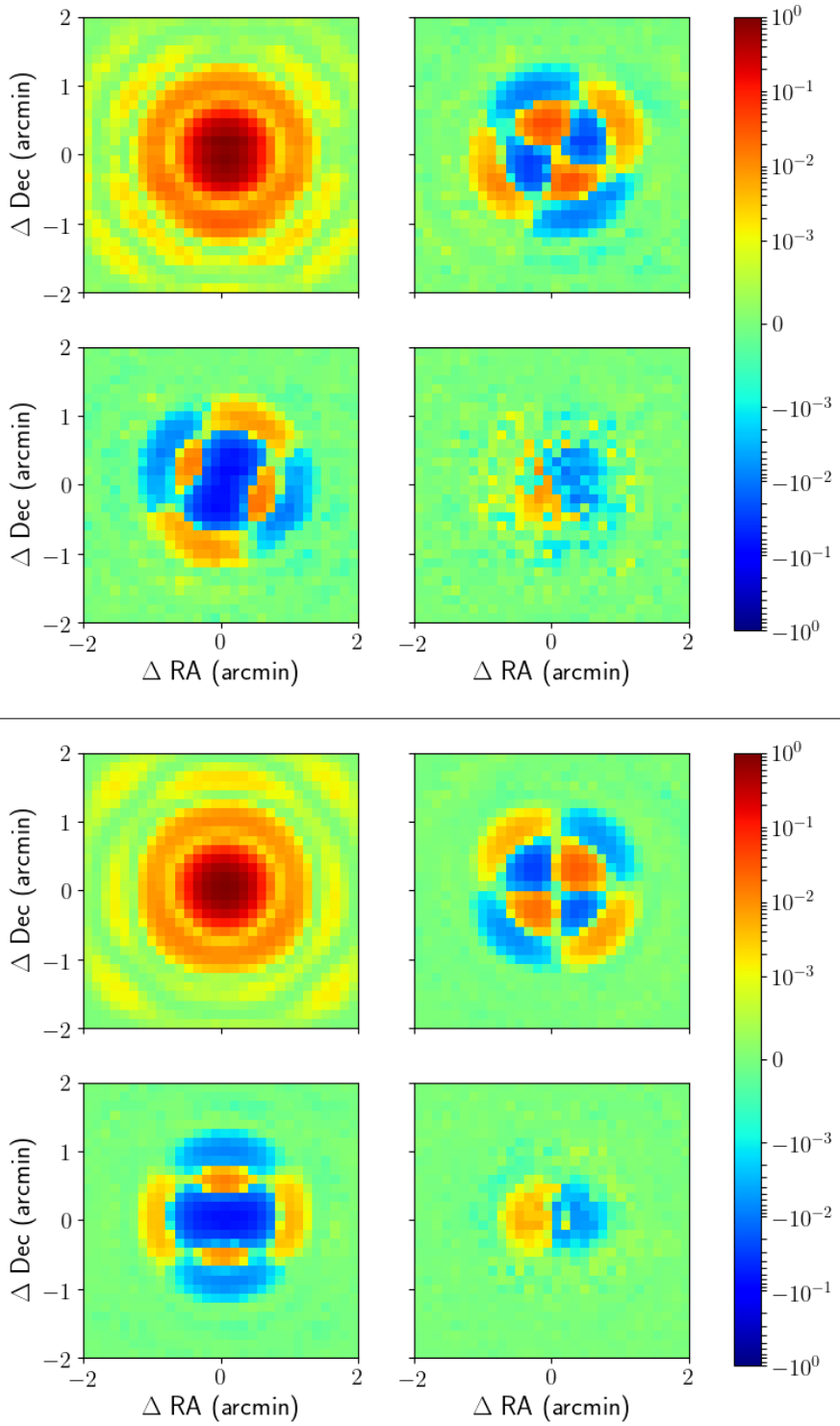

Figure 2.3: **Average PB in Stokes basis:** Holographic map of the ALMA **DV (images above the horizontal line)** and **DA (images below the horizontal line)** antennas in Stokes basis averaged over all antennas in each group and over 2 GHz of frequency band centered at the 108-GHz (Band 3). The four set of images above (DV antenna) and below (DA antenna) show the Stokes-I and -Q patterns in the top row while the bottom row shows the patterns in Stokes-U and -V.

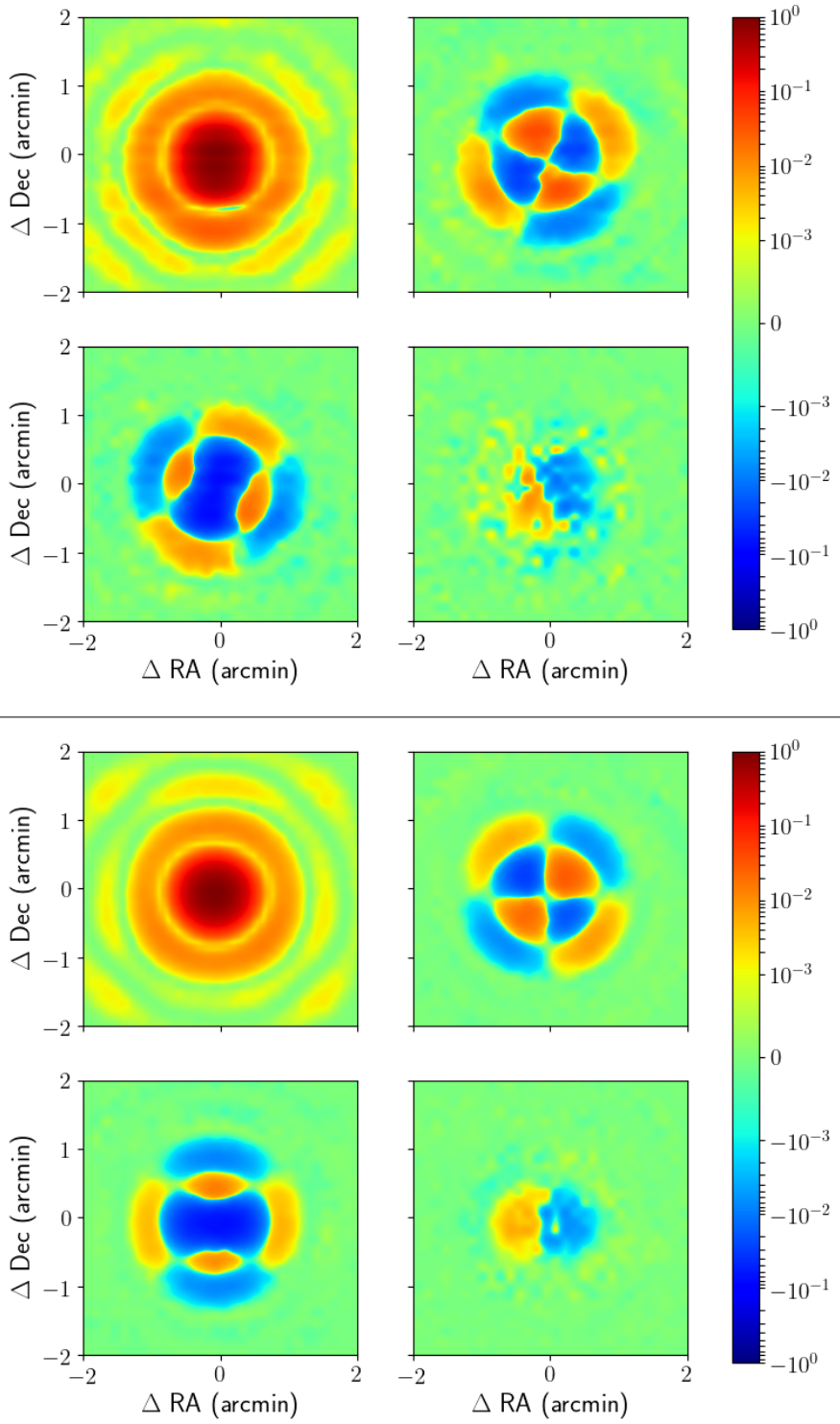

Figure 2.4: **Interpolated Average PB:** The figure shows the interpolated average PBs for the ALMA **DV (images above the horizontal line)** and **DA (images below the horizontal line)** antenna show in Fig. 2.3, interpolated using the cubic spline interpolation technique. The four set of images above (DV antenna) and below (DA antenna) show the Stokes-I and -Q patterns in the top row while the bottom row shows the patterns in Stokes-U and -V.

- Flag any poorly behaving antennas (iterative process)

The Measurement Set (MS) for the data taken in 2015 did not have the standard MS structure. Some of the critical meta information required in the calibration procedure and assumed to be accessible in a pre-defined manner from the MS was in fact not available in this MS. The pipeline infrastructure was therefore written to access the necessary meta data to allow for the calibration of the 2015 data using a release CASA build. For instance, the scanning and tracking antenna positions had to be extracted from the antenna pointing table using the CASA table tool (`tb`). In addition to *deriving* the pointing direction, the time-stamps of the antenna pointing also had to be derived; the closest pointing value for a given antenna for the integration time was used to regrid/interpolate the data from a radial scan onto a regular square grid.

For the 2018 data the need for these additional steps were obviated by the scanning in a regular grid. Since the scans were sequential and row-wise the need to time match was obviated given an antenna subset. More accurate recording of the timing and pointing information leads to few and smaller errors when mapping the measurements from 2018 data to make a map of the antenna PB.

2.3.1 Gridding

Additional software was written to derive the pointing information for the scanning antennas as a function of time to produce PB maps for all polarizations using Eq. 2.3. The data taken in 2015 and 2018 covered the antenna aperture with 15 radial scans of 48 points each and 49x49 point grid **with a grid spacing of 0.2 HPBW per point at 108 GHz** respectively. A number of interpolation schemes were investigated to interpolate these data on a finer grid. In the end, we used the cubic spline interpolation as implemented in the CASA `imregrid` task. The AIP was first computed by Fourier transforming the measured holography voltage patterns, and the apertures were interpolated by a factor of 10 using third order spline curves. These interpolated AIPs were later used to develop the Zernike polynomial-based models of the antenna PBs, as described in Section 3.1. The interpolated PBs (interpolated from holography) in all Stokes parameters from the 2018 data, with an over sampling of 10X compared to the raw data are shown in Fig. 2.4.

The PB maps from the 2015 data showed that the SNR was already too low even in Stokes-I to reliably map the first PB side lobe. For most antennas, the Stokes-V map had just enough SNR to show the expected bipolar pattern. For reasons not very well understood, Stokes-Q and -U maps remained unreliable. The noise is too high and the antenna-to-antenna variations were unrealistic. We speculate that this could be due to the uncertainty in the position,

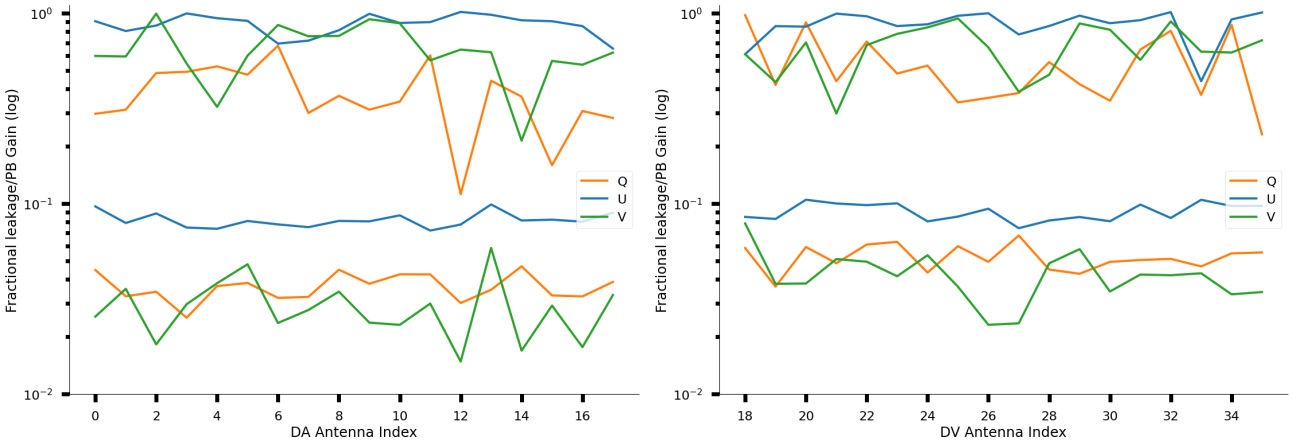

Figure 2.5: **Peak leakages and its location:** Peak of the Stokes-Q, -U and -V patterns for the individual DA (left) and DV (right) antenna groups. The set of three curves in the upper part of the plots show the fractional Stokes-I PB gain at the location of the peak leakages shown in the corresponding (same color) plots in the lower part of the graphs.

which had to be derived (not recorded in the MS) and then interpolated due to the specific manner in which this data was taken.

The data from 2018 was specifically taken to (a) have recorded antenna pointing directions in the MS, (b) improve SNR by higher integration time and (c) scanning a wider angle to as many points as allowed by the available observing time across the AIP. The PB maps from this data shows the positive effects of both, higher SNR and better handle on antenna pointing direction. SNR is high enough to reliably map up to the 4^{th} side lobe in Stokes-I and get reliable maps in all other Stokes parameters (see Fig. 2.4). All Stokes-planes show the expected structure. Stokes-I has the pattern due to aperture blockage from feed legs and secondary reflector. Stokes-Q and -U show the "clover leaf" pattern with the U pattern rotated by 45° with respect to the Q pattern. Stokes-V shows the bipolar pattern.

2.4 Antenna-to-antenna variations

In our processing, we found two axes along which significant antenna-to-antenna variations are seen: in the precise shape of the PB and leakage patterns, and in the antenna pointing offsets.

2.4.1 Beam shapes

The full Stokes beams constructed from the holography measurements are shown in Fig. 2.3. These images were made from the antenna- and frequency-averaged holography data after it was corrected for the residual per-antenna pointing offsets (see Sec. 2.4.2). These beams were interpolated by a factor of 10 to create the images in Fig. 2.4. Figures 4.1 and 4.2 show the frequency-averaged data for the individual DA and DV antennas respectively. These figures show antenna-to-antenna variations in the shapes, orientation and the location of peaks in the leakage patterns. Individual antenna patterns also vary significantly from the average patterns.

The final full-Stokes imaging rely on the precise prediction of the sky model in an iterative image reconstruction algorithm. While the average patterns characterize the Stokes flux vector the image plane, it is the precision of the prediction step that more strongly determine the accuracy in the final science-quality image. This step requires full-Stokes PB models for individual antenna, or an average model if the antenna-to-antenna variations are insignificant. Individual antenna PBs show significant differences between DA and DV antennas. This is expected since the optics of the two antenna types is different. ALMA imaging therefore requires heterogeneous array treatment with at least two groups of antennas (the DA and DV group of antennas). Antennas within each group also show significant variations (Figs. 4.1 and 4.2). It therefore remains to be determined if full-Stokes imaging would require a fully heterogeneous array treatment.

Most antennas show a significant residual leakage at the center of the beam, particularly in Stokes-U. This is unexpected and may be due to residual leakage not modeled and removed as part of the ALMA polarization calibration procedure. The Stokes-V pattern varies in shape and orientation across antennas. This could be due to an uncorrected residual (*i.e.,* post calibration) XY-phase difference. Further investigation is required to nail down the precise reason for these effects.

Figure 2.5 shows peak fractional leakage gains for each antenna in the two groups and the value of the fractional Stokes-I gain at the location of these peaks. Table 2.1 has the numerical ranges of the peak leakages and the range of the gain in the main lobe where the peaks occur.

These variations will affect the imaging performance. If not accounted for, the fractional error on Stokes-Q, -U and -V flux measurements could be at the level of a few 10s of percent and the imaging dynamic range may also be limited. More precise characterization of their impact via careful simulations and full-Stokes imaging experiments will be crucial in developing a path towards ultimately enabling precision and *reliable* full-Stokes wide-field imaging with ALMA.

Ant. type	Stokes type	Range of peak Fractional leakage	Range of position Fractional PB gain
DV	Q	4–7%	20–100%
	U	7–10%	40–100%
	V	2–8%	30–90%
DA	Q	3–5%	10–70%
	U	7–10%	65–100%
	V	1–6%	20–100%

Table 2.1: **Antenna to antenna variation of the peak fractional leakage** in the Stokes-Q, -U and -V patterns shown in Figs. 4.2 and 4.1, and the range of the Stokes-I gain in the main lobe of the PBs at the location of these peaks for PBs

2.4.2 Antenna Pointing Offsets

As mentioned earlier, the derived per antenna PBs showed significant variations across the antennas as well as unexpected morphological features. Since the standard full polarization calibration removed the observed polarization leakage gain at the center of beam (irrespective of the source of the leakage), the most striking feature that is not expected after full polarization calibration was the presence significant leakage at the center of the PB maps. This was ultimately found to be due to the presence of significant antenna pointing offsets, which also varied across the antennas. These were estimated from the raw PB maps and removed before averaging.

The antenna pointing offsets were estimated by fitting a 2D Gaussian to the main lobe of the raw maps of the X and Y Jones terms and measuring the offset between the peak of the fitted Gaussian and the center point of the holography grid scan. This offset was then used to regrid the data for all terms of the Jones matrix. The regridded Jones terms were then used to derive the PBs.

As show in Fig. 2.6, the pointing offset for the majority of the antennas is clustered around an offset about -12% of the HPBW along both the elevation and azimuth axis for DA antennas. DV antennas are clustered around an offset of -9% and -14% of the HPBW for the elevation and azimuth axes respectively. Two antennas in each group are significant away from this cluster of the rest of the antennas. Multiple data points of the same colour in this figure correspond to the offsets across the frequency band. Fig. 2.7 shows the variation of the pointing offset for a few antennas as a function of frequency after subtracting the mean offset. These variations are at the level of a few percent of the HPBW, which may not be significant. However some antennas show significant systematic variation across frequency, the source of which we do not fully understand.

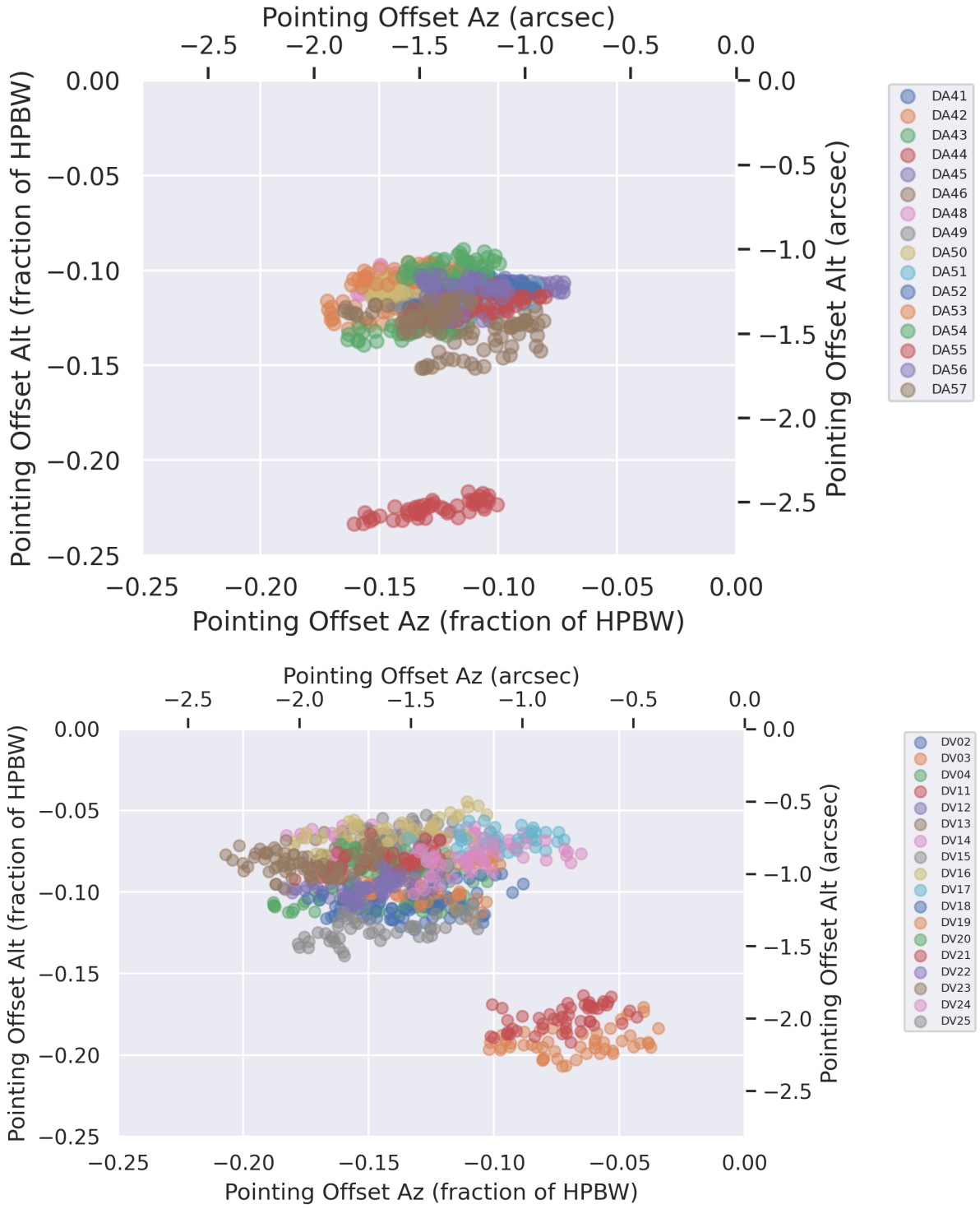

Figure 2.6: **Systematic pointing offsets:** The figure shows the systematic pointing offset derived for all the DA (top panel) and DV (bottom panel) antennas from the holography observations by fitting a 2D Gaussian to the derived X and Y polarizations **across the 2GHz band centered at 108 GHz**. The pointing offsets are represented as a fraction of the antenna HPBW.

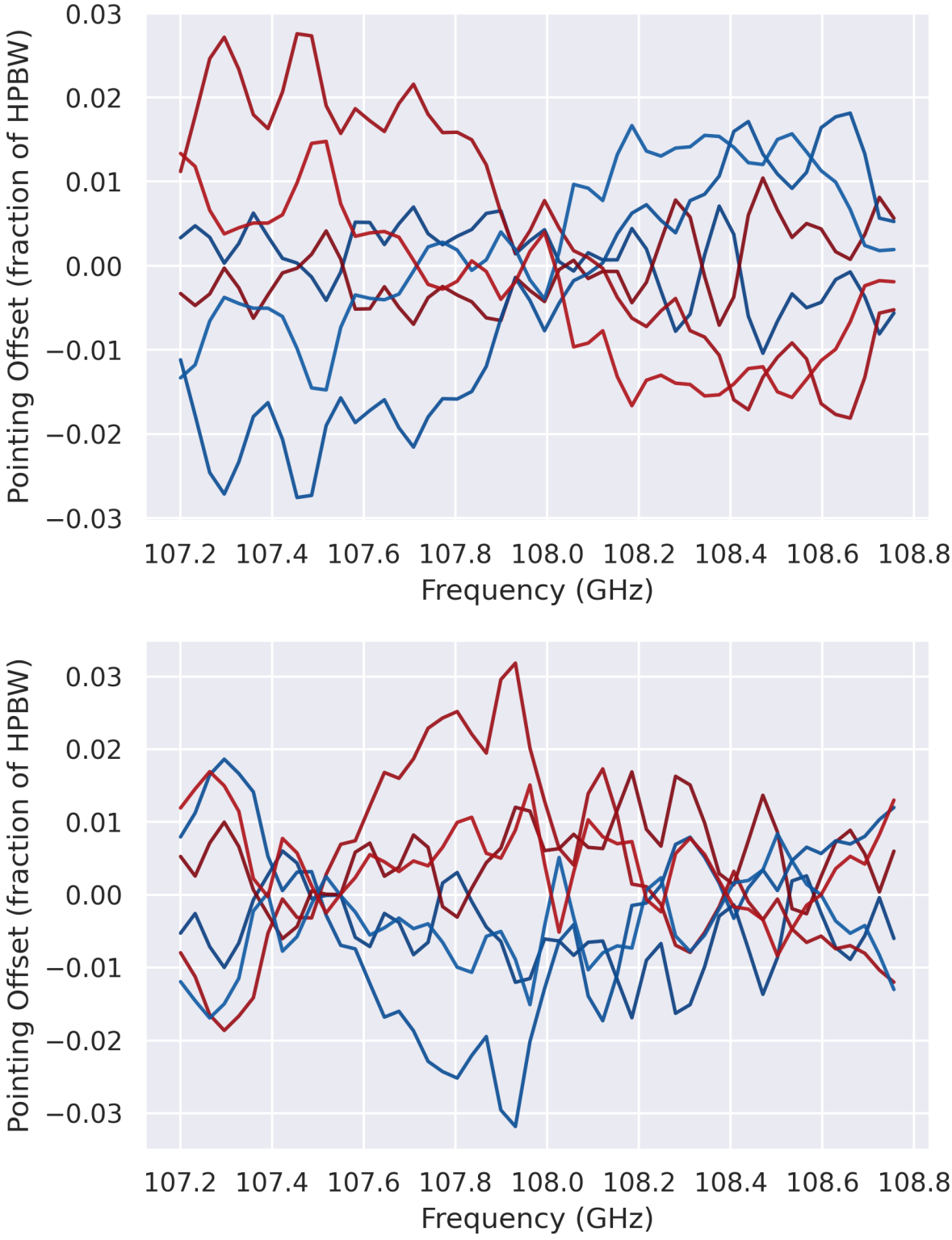

Figure 2.7: **Pointing offsets with frequency:** The figure shows the pointing offset as a function of frequency derived for three DA (top panel) and DV (bottom panel) antennas after removing the systematic pointing offset. The pointing offsets are represented as a fraction of the antenna HPBW. The curves in red are the X polarization and the curves in blue are the Y polarization pointing values. The curves show the presence of a standing wave as a higher harmonic on top of the squint.

Chapter 3

AIP modeling

The model AIP are applied as a convolutional gridding correction in the *A-Projection* framework (Bhatnagar et al. 2008; Jagannathan et al. 2017). The basic approach to arrive at the model of the AIP is to measure the antenna PBs using the technique of antenna holography and Fourier transform them with adequate oversampling in the aperture plane. The resulting oversampled AIP is then modeled in terms of Zernike polynomials and is briefly discussed below (more details in Sekhar et al. (2021)). It is important to point out the advantages of modeling the AIP over modeling the PB. The antenna AIP is a finite function and is physically limited by the dish diameter, unlike the antenna PB which extends well beyond the field of view of the telescope. Furthermore we apply corrections to our observed visibilities, and the AIP characterizes the direction-dependent effects in the visibility domain. This makes the AIP domain the natural domain for our modeling.

3.1 Zernike models

Zernike polynomials are orthonormal polynomials defined on a unit circle. The various Zernike terms correspond to real optical effects (e.g. "piston", tip, tilt, astigmatism, defocus, etc.) and hence are ideally suited to model the AIP. The antenna AIPs obtained from the holography were modeled per spectral window (SPW). The modeling was carried out by fitting the first 10 orders of Zernike polynomials to the AIP using a standard non-linear least squares solver. The AIP model is given by

$$AIP^{M}(\vec{s}) = \sum_{k=0}^{10} \left[A_k^{\Re} + \iota A_k^{\Im} \right] \cdot Z(k, \vec{s}) \tag{3.1}$$

where $\vec{s}$ spans the aperture of a fixed diameter and A_k are the coefficients for the k^{th} Zernike term $Z(k, \vec{s})$. The superscripts $\Re$ and $\Im$ indicate separate coefficients for the real and imaginary parts of the AIP. The objective functions used for deriving the coefficients $A^{\Re}$ and $A^{\Im}$ are

$$\chi^{\Re^2} = \sum_{\vec{s}} \left| \Re \left[AIP^{Holo}(\vec{s}) - AIP^{M}(\vec{s}) \right] \right|^2 \tag{3.2a}$$

$$\chi^{\Im^2} = \sum_{\vec{s}} \left| \Im \left[AIP^{Holo}(\vec{s}) - AIP^{M}(\vec{s}) \right] \right|^2 \tag{3.2b}$$

where AIP^{Holo} is the measured AIP from astro holography observations. The models are fitted in the aperture (visibility) domain independently for the real and imaginary parts and for each of the four Jones terms. Modeling all the terms of the complex antenna Jones matrix this way allows us to reconstruct the entire 4×4 Mueller matrix from the 2×2 Jones matrix constructed from the modeled apertures. The *average* PBs in the Stokes basis generated from these Zernike models are shown in Fig. 3.2 for both DA and DV antenna types. These are constructed by modeling

Ant. type	Stokes type	Peak Fractional leakage	Position Fractional PB gain
DV	Q	4%	33%
	U	8%	90%
	V	1%	60%
DA	Q	3%	33%
	U	7%	88%
	V	1%	50%

Table 3.1: **Antenna-averaged peak fractional leakages** in Stokes-Q, -U and -V patterns shown in Fig. 2.5, and the Stokes-I PB fractional gain at the location of these peaks **as measured at the TDM spectral window central frequency ~108 GHz**

the antenna- and frequency-averaged holography data in order to maximize the SNR during modeling. However we find that the SNR is sufficiently high if we use only frequency-averaged data for each antenna separately, allowing us to generate per-antenna models as well. These beams capture the features of the Stokes PBs very well (the quadrupolar pattern of the Stokes-Q and -U beams and the bipolar pattern of Stokes-V).

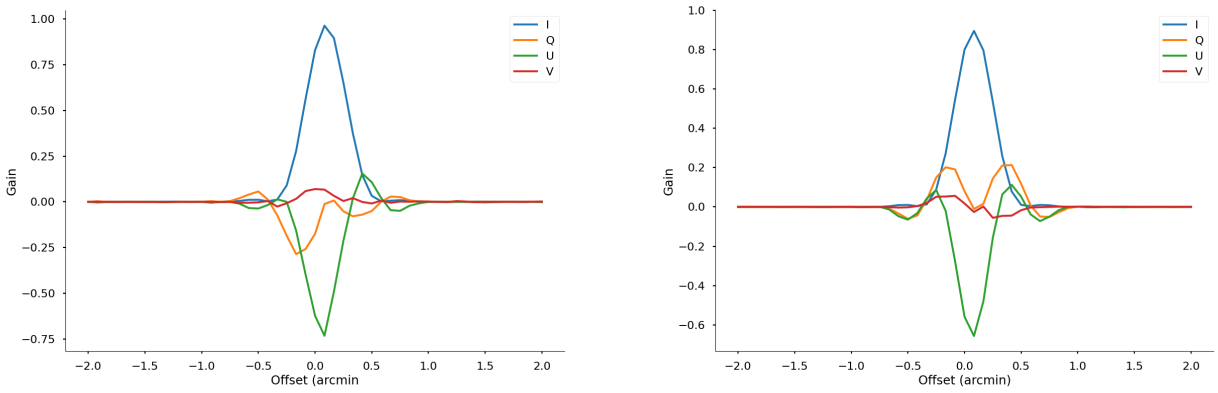

Figure 3.1: **Profile of the leakages and their location:**A slice across the average DV (left panel) and DA (right panel) antennas are plotted for Stokes-I, -Q, -U and -V **at ~108 GHz**. Note that the values of Stokes -Q, -U and -V have been scaled by a factor of 10 for clarity.

Table 2.1 lists the values of the peaks of the leakages in the *average* patterns in Stokes-Q, -U and -V for the DA and DV antenna types, and the PB forward gain where these leakages peak. Figure 3.1 graphically show the shape and angular extend of the fractional leakage compared to the extend of the main lobe of the Stokes-I pattern for both antenna types.

As noted earlier, modeling in the aperture domain has the advantage over modeling in the PB domain in that the total size of the aperture is fixed, as opposed to the PB where the sidelobes can extend significantly further out than the main lobe. Although the models were generate over the antenna averaged SPW, in principle the modeling can be carried out per channel, per antenna allowing for per-baseline beams to be constructed. However with the current holography the SNR is too low per channel to carry out such an exercise.

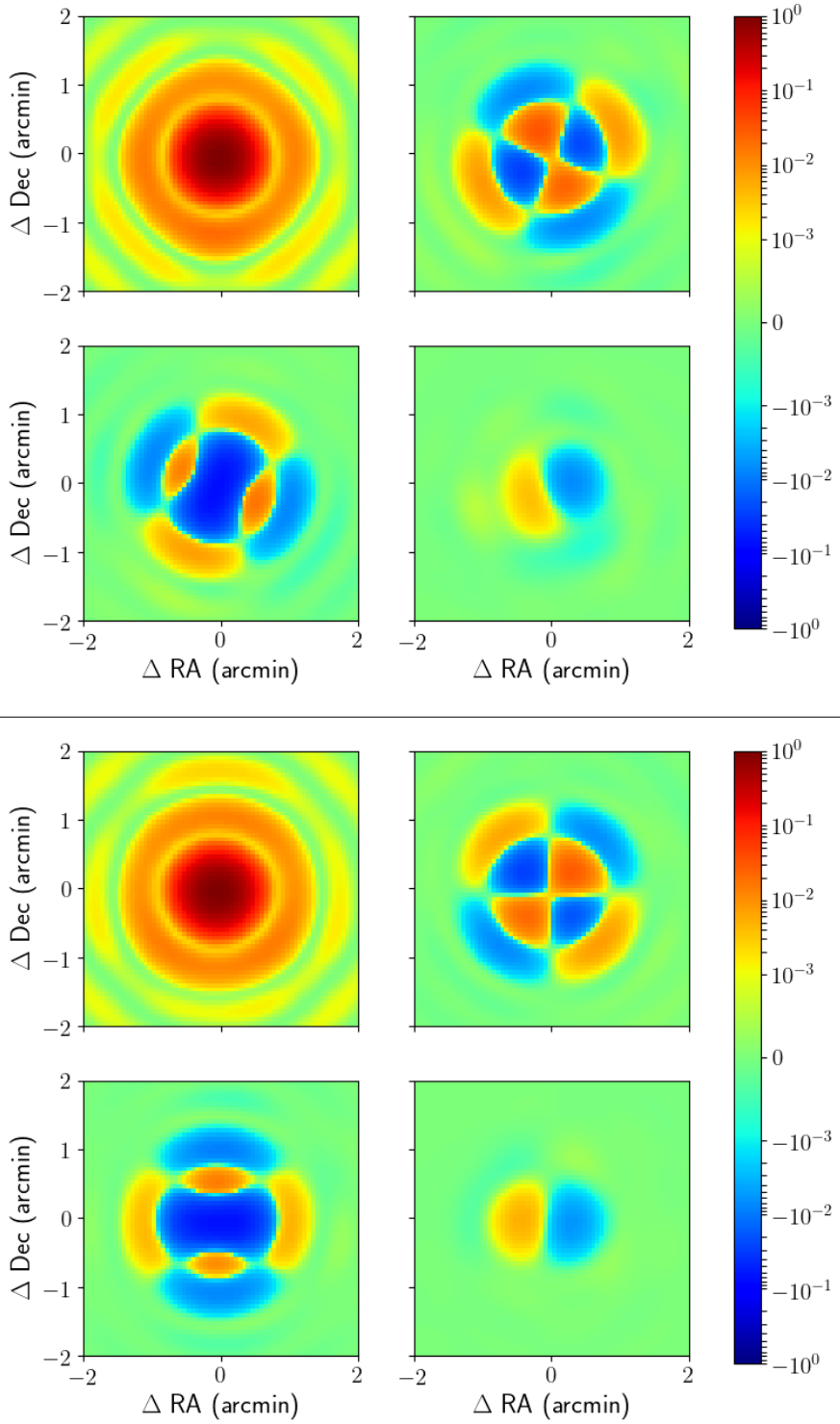

Figure 3.2: **Zernike models:** The Zernike models for the first row of the Mueller matrix for an **average** ALMA DV (above the horizontal line) and **an average** DA (below the horizontal line) antenna in Band 3. The quadrupolar pattern in Q←I and U←I and the bi-polar pattern of V←I are captured in the model. The models are accurate to a few percent within the main lobe for all Mueller elements.

Feed Location Offsets(mm)		
Band	Feed X	Feed Y
1	-180.3	180.3
2	-180.3	-180.3
3	54	-306
4	54	306
5	173.2	-173.2
6	173.2	173.2
7	100	0
8	0	-100.3
9	0	100
10	-100	0

Table 3.2: Table of the locations of all the antenna feed centers used in the Ray-Tracing code.

3.2 TICRA beam models

Models from TICRA for the DV and DA antenna types exist as pixelated images of the antenna EFPs. These were generated using standard techniques for modeling antenna beams for idealized antenna structure. These therefore represent the *ideal* patterns and does not reflect the situation in the field where the actual scientific observations are made. In particular, they cannot capture any antenna-to-antenna variations. Furthermore, since these models exist only as pixelated images, they are not particularly useful for use in imaging algorithms like the *A-Projection* which require evaluation of the antenna AIP at resolutions determined by the specific observation setup. Nevertheless, for completeness we converted the existing EFPs from feed basis to power patterns in Stokes basis using the exact same software that was used for converting holography data to Stokes patterns. These are shown in Fig. 4.3. While the morphological structure in all Stokes planes look reasonable (with a notable exception of the leakage pattern in Stokes-Q for the DV antenna type), the numerical values are not reasonable. In particular the off-axis leakage patterns (the off-diagonal elements of the antenna Jones matrix) are inconsistent with the measured ones by almost 2 orders of magnitude. At this time, we do not understand the source of these severe inconsistencies in the TICRA models of full-Stokes patterns (in particular the Stokes Q←I, U←I and V←I patterns). For these reasons, we did not further consider these models for developing techniques for wide-field full-Stokes imaging.

3.3 Ray traced ALMA beams

In an effort to recreate the antenna EFPs from the TICRA beams we developed an ALMA antenna model to be used with the built-in code for ray-tracing within the `TCLEAN` framework in CASA. In order to do that we derived the receiver positions as offsets from the center of the cassegrain ALMA DA and DV type antennas. The position and the feed offsets from the central ring that were used and tested for this code are shown in Tab. 3.2. We then generated the ray tracing code modeled along the lines of `BEAMCALC` within the AW-Projection framework. With the infrastructure code in place we generated EFPs for the ALMA antennas and propagated them to generate antenna PB's for all the Stokes parameters. We found that the derived leakages off-axis did not compare in the magnitude with the observed holography data. In order to make the leakage magnitude be comparable required an arbitrary scaling of the observed EFPs off-axis. A similar limitation has limited the use of the ray-tracing code as is for polarization corrections in AW-Projection in the past Jagannathan et al. (2018). We therefore decided to not pursue this line of research further and instead proceed with the polynomial based modeling technique that better represents the observed holography data.

Chapter 4

Appendix

4.1 Data

The holographic data were collected in October of 2018 in ALMA Band-3. The observations were split into six observing block IDs, each containing a scan of the calibrator source J1924-2914, which acted us the flux, bandpass and polarization calibrator as well. A second scan containing the holographic grid pattern is also present in each observing block ID. The observations spanned ∼ 60 degrees in parallactic angle of the calibrator source to allow

Band	Obs Block id	Tracking Antennas	Scanning Antennas
Band 3	*uid___A002_Xd2d9a0_X8dd3*	DV02 DV03 DV04 DV11 DV12	DA41 DA42 DA43 DA44 DA45
	uid___A002_Xd2d9a0_X92ae	DV13 DV14 DV15 DV16 DV17	DA46 DA48 DA49 DA50 DA51
	uid___A002_Xd2d9a0_X991e	DV18 DV19 DV20 DV21 DV22	DA52 DA53 DA54 DA55 DA56
		DV23 DV24 DV25	DA57 DA58 DA59
Band 3	*uid___A002_Xd2d9a0_X8f4c*	DA41 DA42 DA43 DA44 DA45	DV02 DV03 DV04 DV11 DV12
	uid___A002_Xd2d9a0_X9427	DA46 DA48 DA49 DA50 DA51	DV13 DV14 DV15 DV16 DV17
	uid___A002_Xd2d9a0_X9b2e	DA52 DA53 DA54 DA55 DA56	DV18 DV19 DV20 DV21 DV22
		DA57 DA58 DA59	DV23 DV24 DV25

Table 4.1: **Table of observations :** The table shows the observations that provided the holographic data used in this report. The table contains the observation block IDs for the three scans of the holographic grid and the corresponding reference and scanning antenna being used.

for full polarization calibration following the standard ALMA polarization processing recipe. The observations also ensured that we have scans where one set of antennas were scanning the holographic grid while the others were tracking the calibrator at the center of the grid. We obtained another set of measurements where the scanning and the tracking antennas were switched, thus ensuring that we could map out the holographic beams of the entire array available to us. With our calibration and processing pipelines that were developed as part of this study project we could process the data and produce holographic beams within 24 hours to provide preliminary results to all members of the group.

4.2 Per antenna PBs

Following figures show the first row (or column) of the Mueller matrix for each scanning antenna in the holography data. Each figure contains multiple panels, with the images in each row corresponding to Stokes-I beam and the Q←I, U←I and V←I leakage patterns. Significant variations between the antennas in the same group (DV or DA antenna types) as well as between the antenna group is clearly seen.

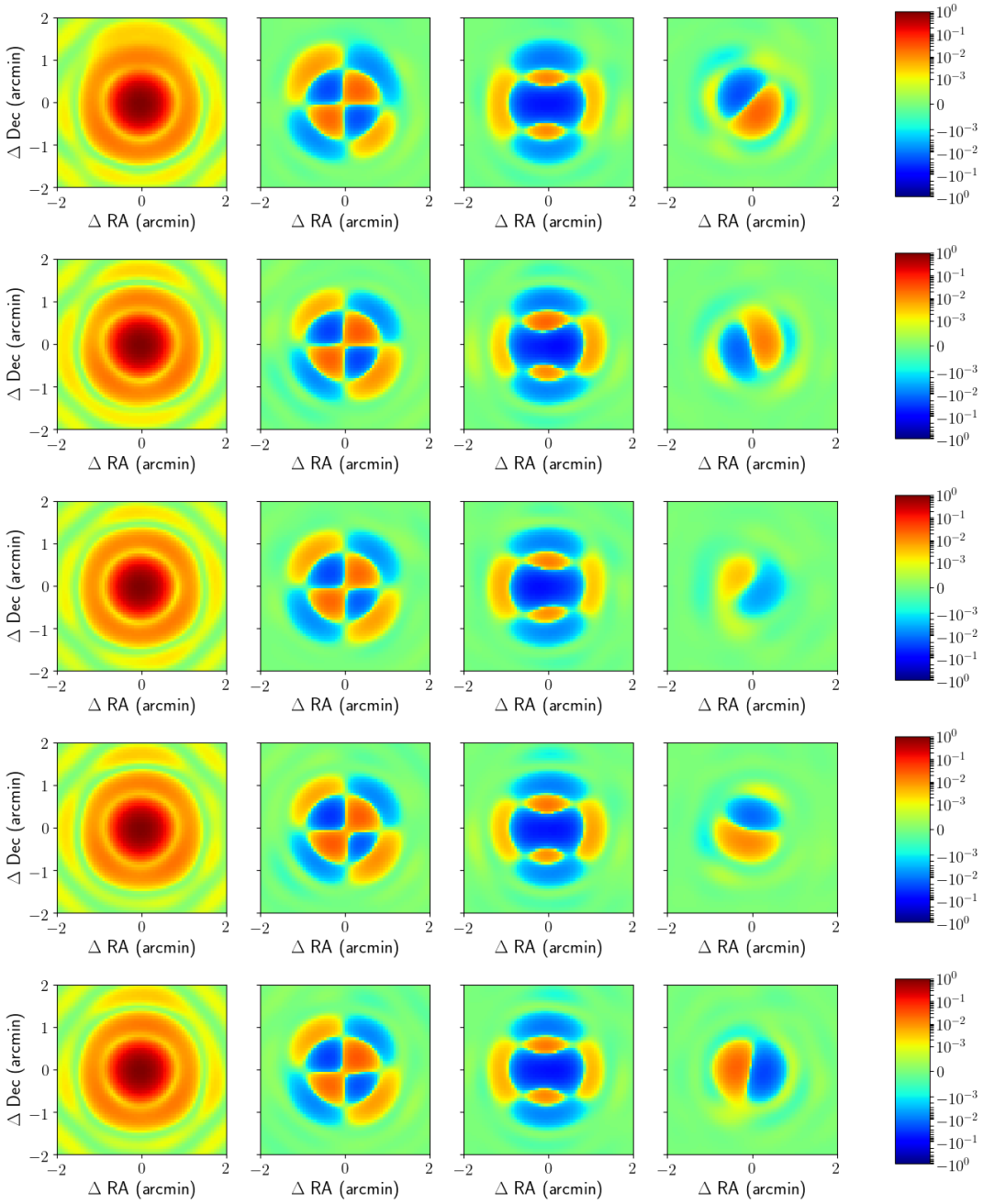

Figure 4.1: **1: DA antenna variations:** Each panel shows the first row of the Mueller matrix constructed from the Zernike models of the various ALMA DA antennas, illustrating the antenna-to-antenna variations of the beams.

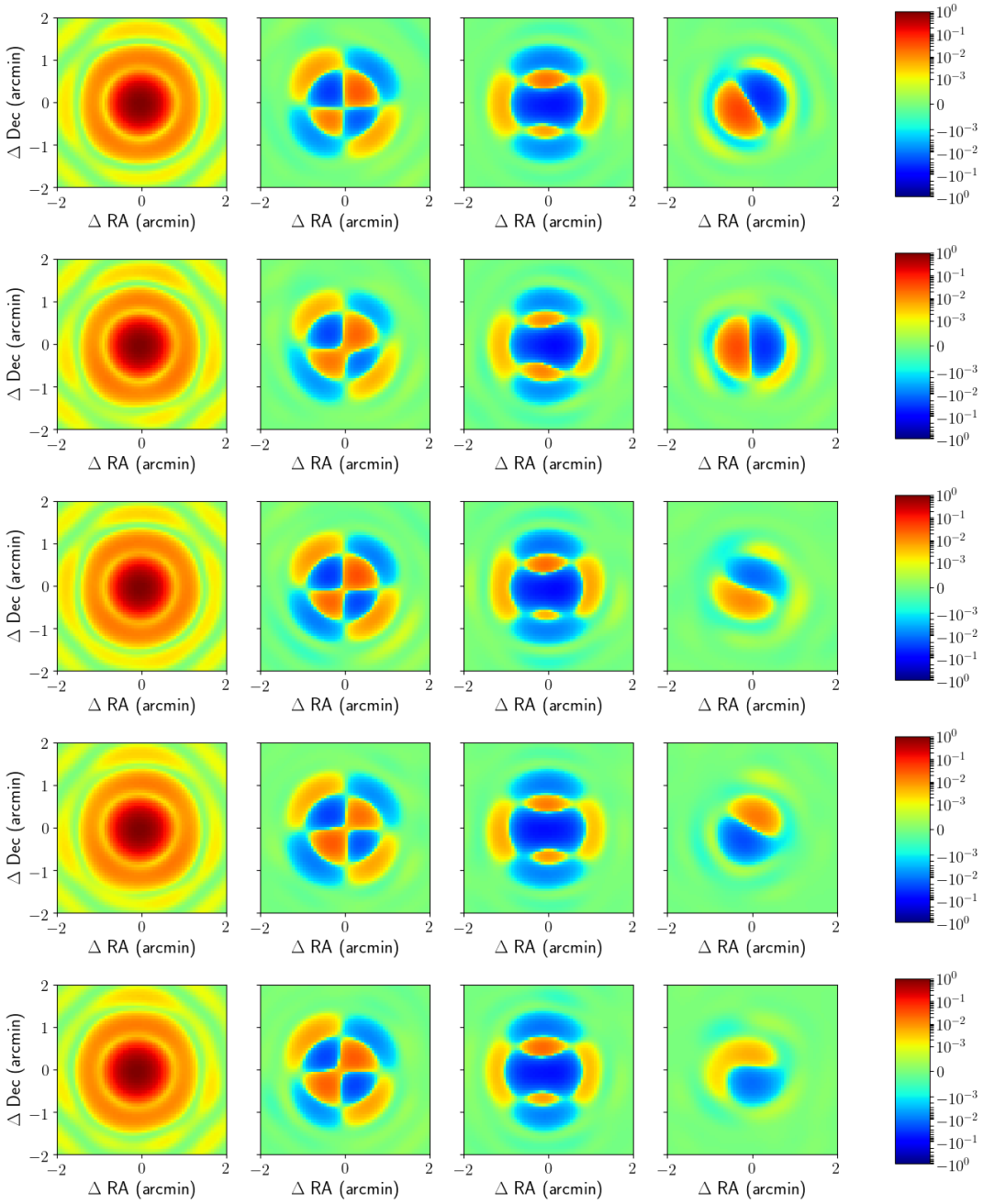

Figure 4.1: **2: DA antenna variations:** Each panel shows the first row of the Mueller matrix constructed from the Zernike models of the various ALMA DA antennas, illustrating the antenna-to-antenna variations of the beams.

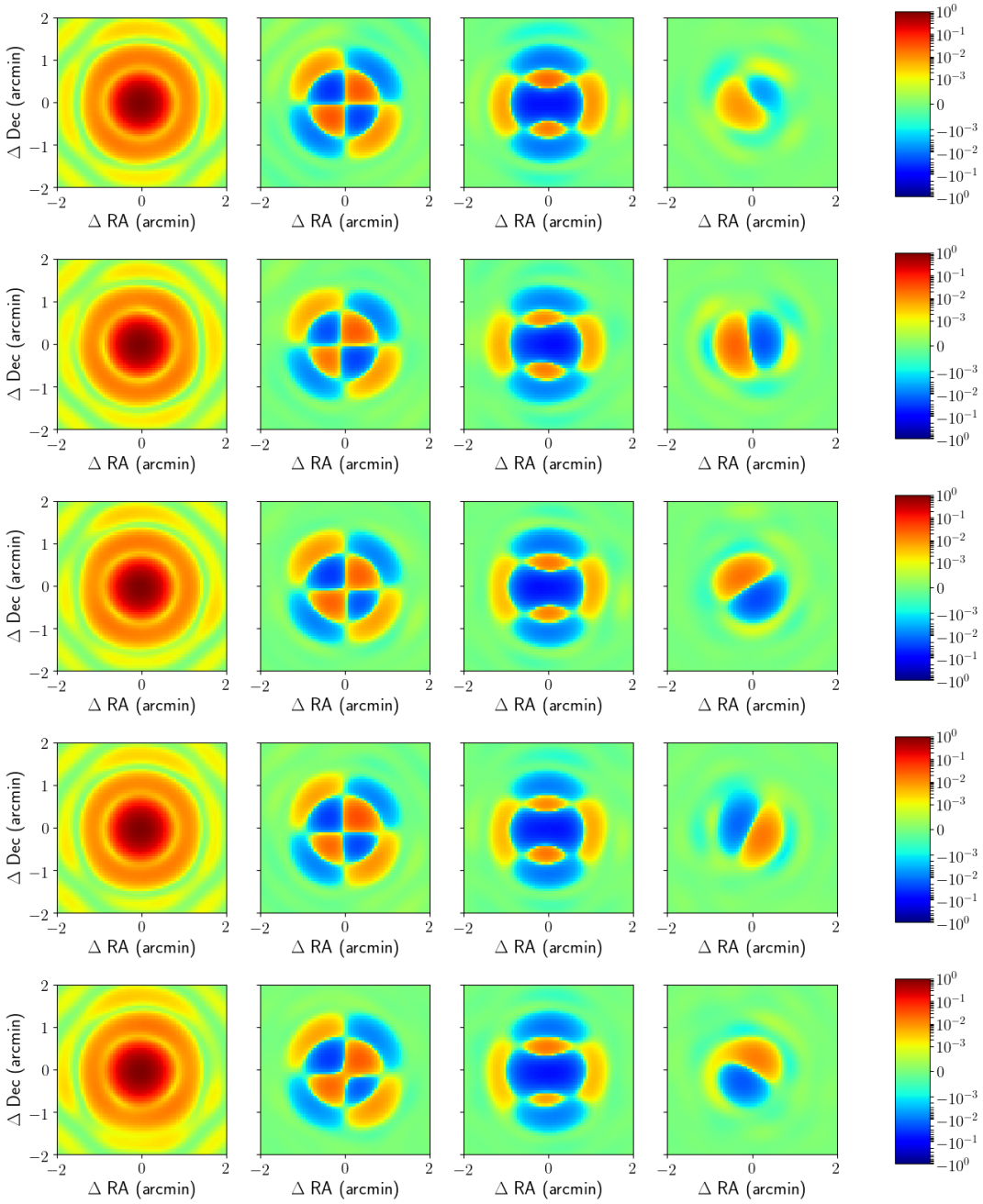

Figure 4.1: **3: DA antenna variations:** Each panel shows the first row of the Mueller matrix constructed from the Zernike models of the various ALMA DA antennas, illustrating the antenna-to-antenna variations of the beams.

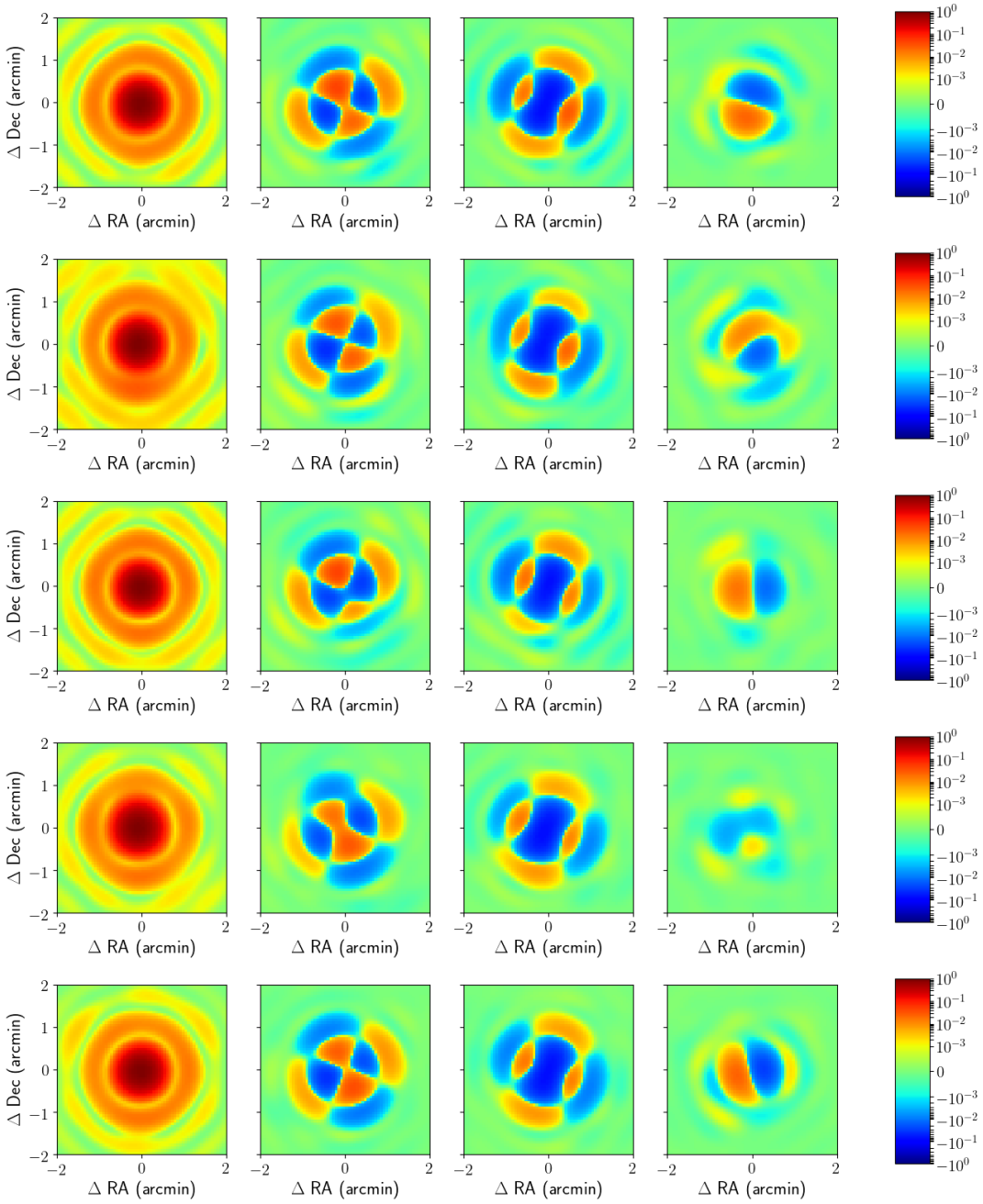

Figure 4.2: **1: DV antenna variations:** Each panel shows the first row of the Mueller matrix constructed from the Zernike models of the various ALMA DV antennas, illustrating the antenna-to-antenna variations of the beams.

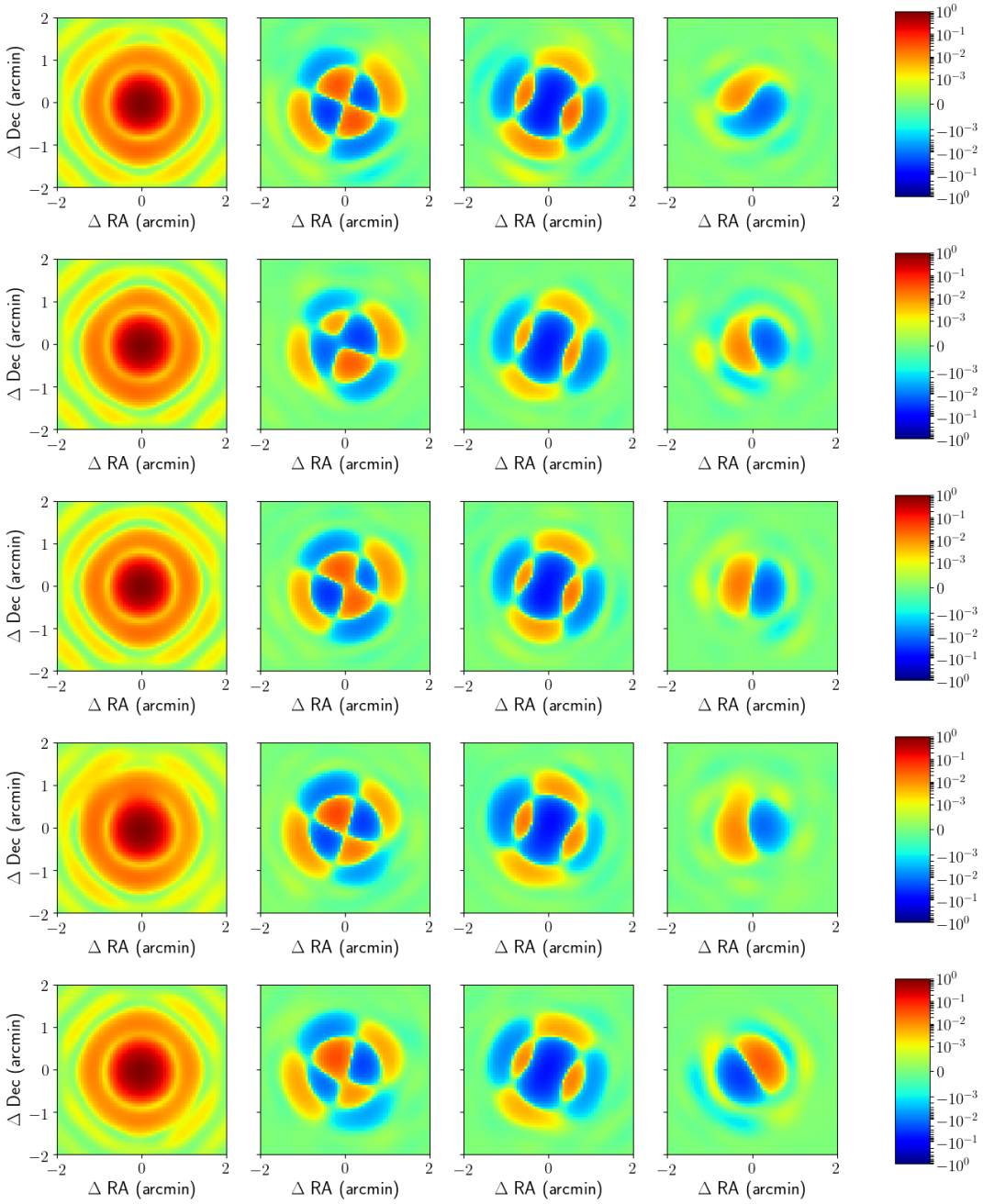

Figure 4.2: **2: DV antenna variations:** Each panel shows the first row of the Mueller matrix for the various ALMA DV antennas, illustrating the antenna-to-antenna variations of the beams.

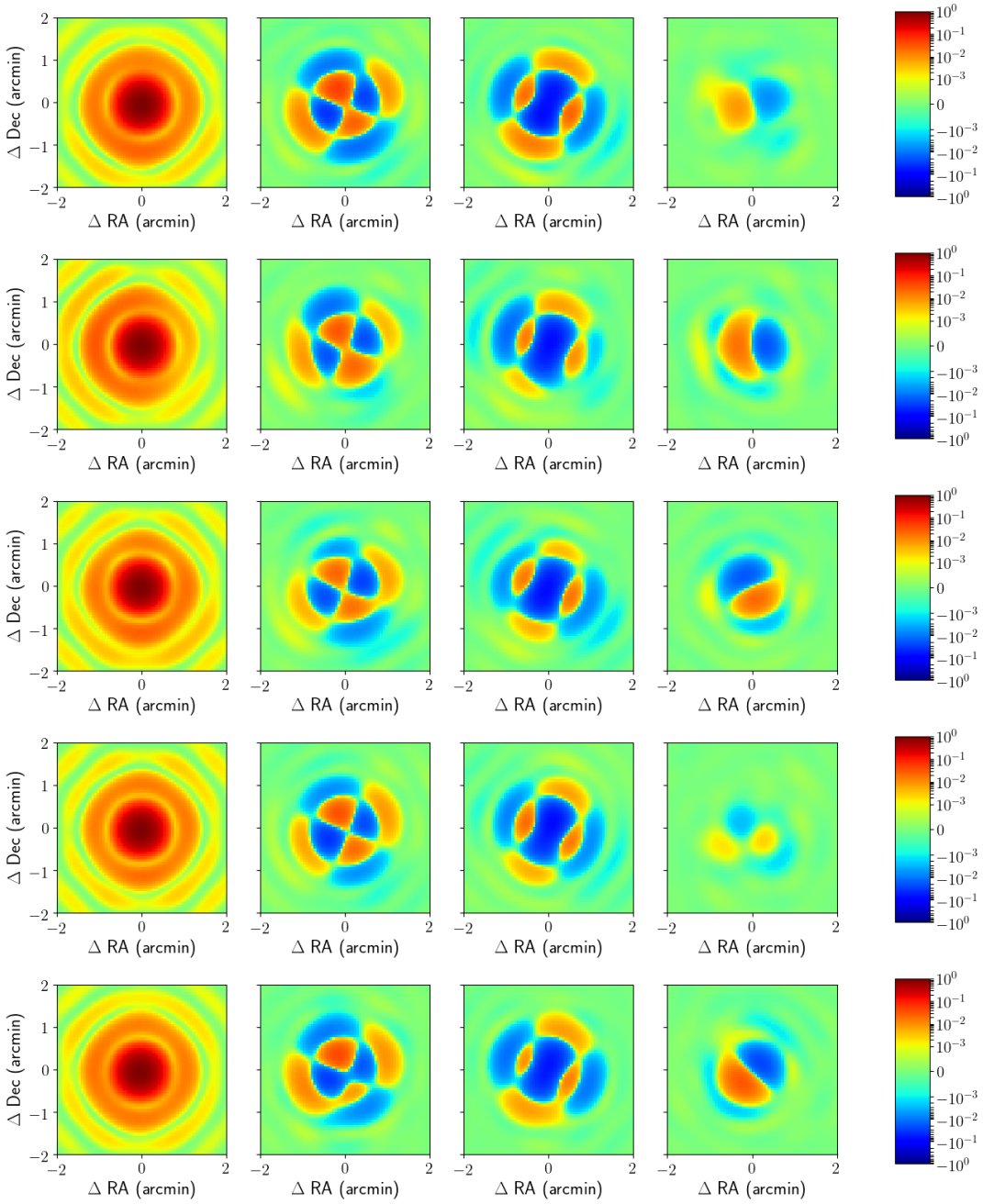

Figure 4.2: **3: DV antenna variations:** Each panel shows the first row of the Mueller matrix constructed from the Zernike models of the various ALMA DV antennas, illustrating the antenna-to-antenna variations of the beams.

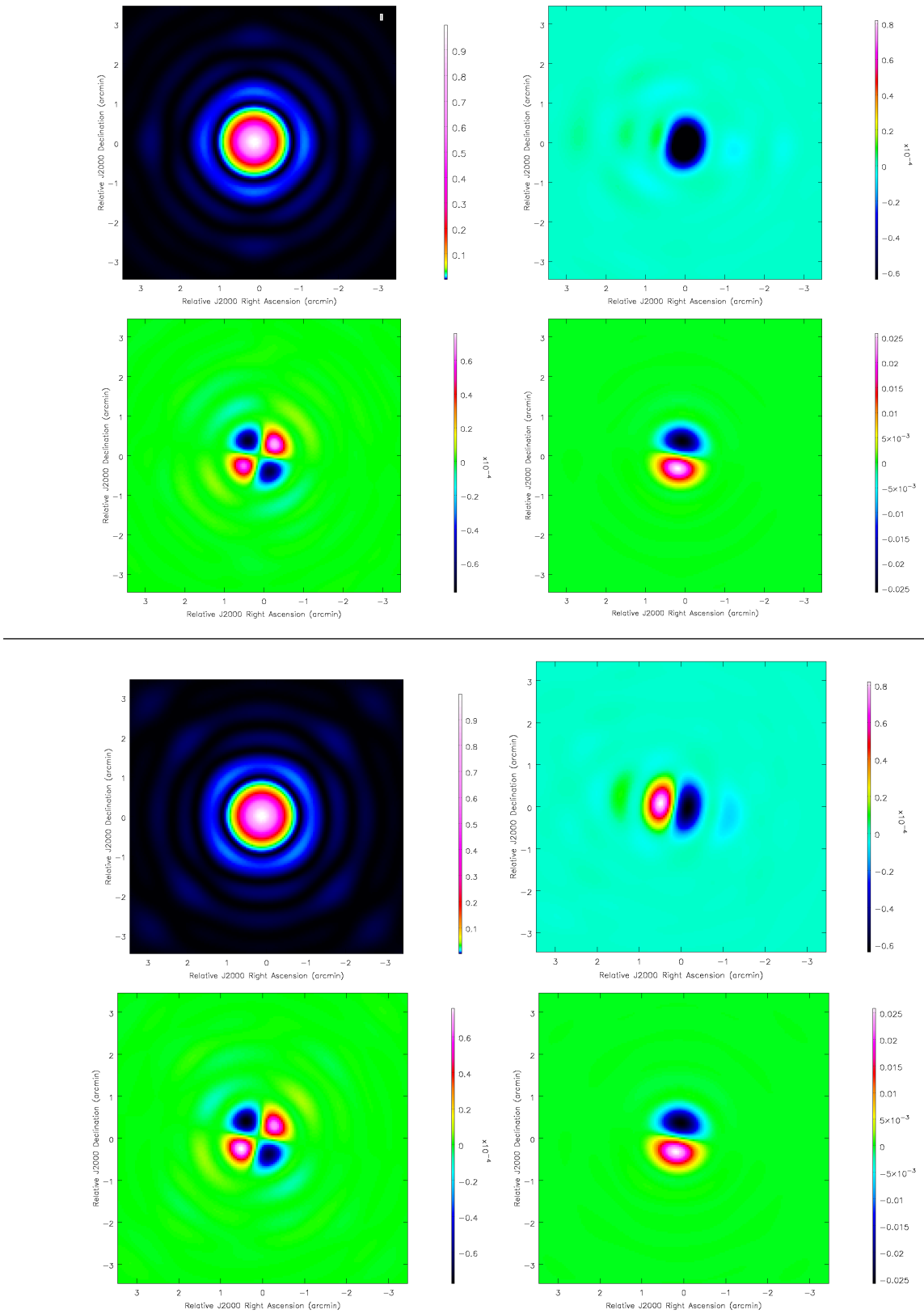

Figure 4.3: **TICRA models:** The TICRA models for the first row of the Mueller matrix for an ALMA DV (above the horizontal line) and DA (below the horizontal line) antenna in Band 3. The top row in each panel shows the Stokes-I and -Q beams while the bottom row shows the Stokes-U and -V beams. Note that the colorbars for Stokes-Q and -U are multiplied by 10^{-4}.

Chapter 5

Bibliography

Bates, R. H. T. 1971a, Int. J. Engng. Sci., 9, 1107

Bates, R. H. T. 1971b, Int. J. Engng. Sci., 9, 1193

Bhatnagar, S., Cornwell, T. J., Golap, K., & Uson, J. M. 2008, A&A, 487, 419

Jagannathan, P., Bhatnagar, S., Brisken, W., & Taylor, A. R. 2018, The Astronomical Journal, 155, 3

Jagannathan, P., Bhatnagar, S., Rau, U., & Taylor, A. R. 2017, The Astronomical Journal, 154, 56

Kundert, K., Rau, U., Bergin, E., & Bhatnagar, S. 2017, IEEE Transactions on Antennas and Propagation, 65, 644

Sekhar, S., Jagannathan, P., Kirk, B. M., Bhatnagar, S., & Taylor, A. R. 2021, in preparation